Design of A Novel 3D Tip-based Nanofabrication System with High Precision Depth Control Capability

Yanling Tian[a,b,*], Kangkang Lu[a], Fujun Wang[a], Zhiyong Guo[c], Chongkai Zhou[a], Cunman Liang[a], Yanjie Yuan[a], Dawei Zhang[a]

[a] *Key Laboratory of Mechanism Theory and Equipment Design of Ministry of Education, Tianjin University, Tianjin 300072, China*
[b] *School of Engineering, University of Warwick, Coventry CV4 7AL, UK*
[c] *Aeronautical Engineering Institute, Civil Aviation University of China, Tianjin 300300, China*

Abstract

The design, analysis, and experimental investigation of a novel 3D tip-based nanofabrication system with high precision depth control capability is presented in this paper. Based on this system, a new depth control method, namely tip displacement-based closed-loop (DC) depth control methodology is proposed to improve the depth control capability. As the force-depth prediction with the commonly-used depth control method, i.e. the normal force-based closed-loop (FC) method, may depend on the machining speed, the machining direction, and the material properties, etc. Compared with the FC method, the DC method decreases the complexity and the high uncertainty. The tip feed system utilizes a non-contact force, i.e. the electromagnetic force, to adjust the tip displacement. Therefore, the tip support mechanism can be used to accomplish the tip-sample contact detection. Additionally, an active compensation method is proposed to eliminate the tilt angle between the sample surface and the horizontal plane. Otherwise the machining depth will change gradually, i.e. getting deeper or lower. Furthermore, a series of patterns have been fabricated on silicon sample surface with the proposed system and method. The maximum machining depth of a single scan reaches 300 nm, which is much larger than that of an

*Corresponding author
Email address: meytian@tju.edu.cn (Yanling Tian)

atomic force microscope (AFM)-based nanofabrication system. The experimental results demonstrate that the system has advantages of distinguished depth control capability, high machining accuracy, and excellent repeatability, which diminishes the influence of above-mentioned factors on the machining depth. Also, the method has the potential of machining arbitrary 2D/3D patterns with well-controlled depth and high accuracy.

Keywords: Tip-based nanofabrication, Nano manufacturing, Nano fabrication

1. Introduction

Applications with micro/nano scale characteristics have been used in many academic and industrial fields, such as semi-conductor, biomedicine, and many more[1–5]. These applications lead the demand for the development of nanofabrication capability. Up to now, several methods have been proposed to fulfill the increasing requirement with different principles, including electron beam lithography (EBL)[6], focused ion beam (FIB)[7], femtosecond laser machning[8], ultraviolet light lithography[9], X-ray lithography[10], nanoimprint[11], tip-based nanofabrication (TBN)[12–18], and other special methods[19, 20]. Among all these methods, TBN technology possesses nano resolution machining capability, along with several unique advantages in term of low cost, simple principle, ease of use, etc.

Machined surfaces with micro/nano scale patterns can be used for DNA or macromolecular analysis[1, 21], drug delivery[22], droplet generation[23], and so on.[24] As functional units, the nanochannels are essential components in micro/nanofluidic systems. To fabricate the nanoscale components, several fabrication techniques have been investigated, including photolithography[23, 25], e-beam lithography[26, 27], and nanoimprint[28, 29]. These techniques can fabricate nanoscale patterns with controlled features. Also, the photolithography and nanoimprint techniques have the capacity for mass production. However, the high cost of photolithography and e-beam lithography can not be ignored. Moreover, the flexibility of nanoimprint technique is limited, as the master pat-

tern must be re-designed and re-machined for a small change. Hence, the TBN method provides a low-cost and flexible method for fabricating nanoscale patterns. Furthermore, it can be used to fabricate the master pattern for nanoimprinting.

TBN technology appeared along with the development of scanning tunneling microscopy (STM)[30]. Some patterns were observed on the surface of a measured sample, which turned out to be tip induced surface local oxidation. However, as another kind of scanning probe microscopy, the atomic force microscope (AFM) provides better choice in realizing TBN technology. Compared with STM, AFM can work in ambient environment, and machine on metal or nonmetal materials. Moreover, AFM is easier to combine with other approaches, like electrical, chemical, and thermal methods, to establish an integrated compound nano fabrication system[31–34]. However, the compound machining system needs more complicated structure, and can only machine patterns on specific materials. Therefore, AFM-based mechanical scratching method is more commonly used for its simplicity and multiple material suitability.

AFM was initially designed for measuring surface topography, a silicon tip with a radius of tens of nanometers is used. The tip is fixed on the holder with a rectangular cantilever (length: hundreds of μm, width: around 10 μm, thickness: 0.5 μm - 5 μm). The stiffness of the cantilever is about several Newton per meter. The low-rigidity of the cantilever is used to ensure the sensitivity of the force detection. However, cantilevers with low stiffness are vulnerable to environmental changes when using in nano fabrication, this limits the system's dynamic performance. Furthermore, the maximum normal force provided by AFM is not enough to machine hard materials and to achieve a high-speed fabrication. One solution to this problem is adopting high-stiffness cantilevers[35]. But the large difference of AFM cantilever's stiffness in the longitudinal direction and in the transverse direction leads to different depths in the different machining directions. In addition, the deformation of the cantilever is monitored to detect the normal force applied to the sample surface during the machining process. A closed-loop controlled normal force is realized by

the extension and retraction of the piezoelectric tube. Therefore, the normal force-based closed-loop (FC) depth control method is adopted to control the depth of material removal. This leads to a result that the machining depth can be affected by a series of factors, such as the magnitude of normal force, the machining speed, the machining direction, and the material properties[36]. Hence, the depth control's complexity and the high uncertainty are critical issues of the FC nano fabrication method.

To solve this problem, the tip displacement-based closed-loop (DC) depth control method can be utilized to directly control the machining depth. Gozen and Ozdoganlar established a nano milling system[37]. By attaching the AFM tip (i.e., the nanotool) directly onto an acrylic post in a reverse configuration, the tip is directly supported by the nanotool post. Since the compliant AFM cantilever is not used as the connection element, a high stiffness nanotool assembly is obtained. The machining depth uncertainty is diminished by this DC method. However, the milling system is relatively complicated and costly, as three laser sensors are adopted to establish the reference frame. of the sample surface.

In this paper, the design of a novel 3D tip-based nanofabrication system with high precision depth control capability is presented. The tip feed system utilizes non-contact force, i.e. the electromagnetic force, to adjust the tip displacement. Therefore, the tip support mechanism can be used to accomplish the tip-sample contact detection. The novel design simplifies the aforementioned complexity of the TBN system and the procedures of DC method. Also, an active compensation method is proposed to eliminate the tilt angle between the sample surface and the horizontal plane, otherwise the machining depth will change gradually, i.e. getting deeper or shallower. The experimental results demonstrate that the TBN system has advantages of outstanding depth control capability, high machining accuracy, and excellent repeatability. Additionally, the DC method diminishes the complexity and high uncertainty of the force-depth prediction, which may depend on removal speed, direction, and material properties within the FC depth control technique.

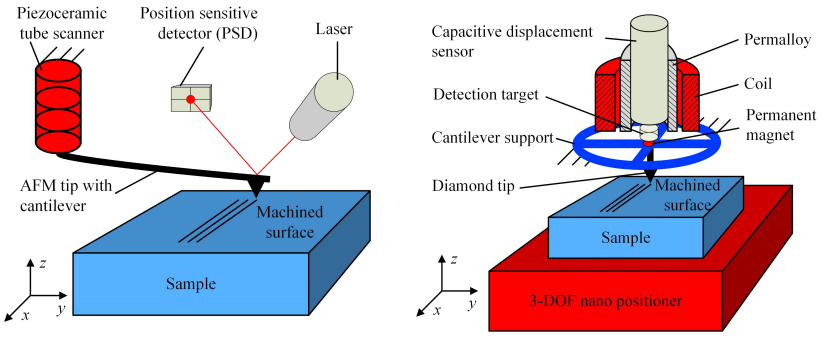

(a) (b)

Fig. 1. Fabrication principles of (a) the FC method, and (b) the DC method

The rest of this paper is arranged as follows. Firstly, the principle of the DC method and the structure of the established system are introduced in Section. 2 and Section. 3, respectively. Then the main machining procedure is listed and explained in Section. 4. The experimental investigation results and discussion are introduced in Section. 5. Finally, the discussions and conclusion are made to further improve the proposed machining ability of mechanical scratching in the future.

2. Comparison of the DC method and the FC method

The principle of the FC method is illustrated in Fig. 1(a). It can be realized by refitting the commercial AFM, i.e. by replacing the tip with another one with higher stiffness. Driven by the piezoceramic tube scanner, the AFM tip approaches the sample surface until the deformation of the cantilever, obtained by the position sensitive detector, reaches a given value. Through maintaining the deformation of the cantilever, a dynamically constant normal force is exerted on the sample surface. By actuating the tip in the horizontal plane, mechanical grooves can be machined. However, it has been found that a series of factors can lead to the variation of machining depth, e.g. the magnitude of normal

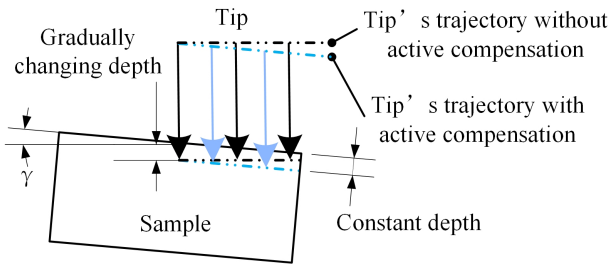

Fig. 2. Schematic diagram of inclination of the sample surface and the active compensation

force, the machining speed, the machining direction, and the material properties. Therefore, it's hard to achieve uniform depth of the machined patterns.

In order to solve this problem, the DC method is proposed as indicated in Fig. 1(b). Instead of controlling the machining depth indirectly with normal force, the position of the diamond tip is directly controlled and measured with interaction force between the electromagnet coil and a permanent magnet. A cross-shaped tip support mechanism is utilized to provide flexibility in the z direction to accompolish the tip-sample contact detection, and provide a high and uniform stiffness in all horizontal directions. The position of the tip is measured by a capacitive displacement sensor. Through this approach, the complicated factors on machining depth mentioned above can be reduced and/or eliminated. Therefore, complicated 2D/3D patterns with accurate depth can be machined at a time, which reduces the control difficulty and improves the machining efficiency.

However, an issue derived from the DC method needs to be addressed, namely, the alignment of the sample surface. As shown in Fig. 2, due to the assembly errors, it is unlikely that the sample surface is always perfectly perpendicular to the tip. Therefore, there is always small tilt error that must be corrected. Also, there exists a tilt angle between motion axis of the positioning stage and the horizontal plane. If the tip position is maintained in the initial place, the depth of machining patterns will change gradually, i.e. getting deeper or shallower. For this reason, Gozen, B. A. and Ozdoganlar, O. B.[37] built an

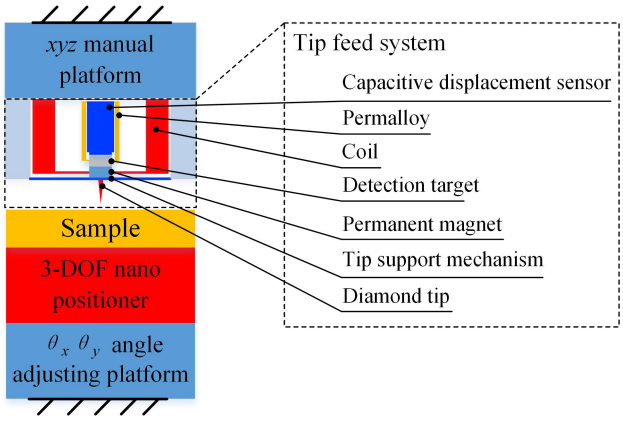

Fig. 3. Schematic diagram of the TBN system

LDV-based three-dimensional (3D) motion measurement system, which is complicated and expensive. In this paper, an alternative method is established, namely, active compensation method (ACM), which will be introduced fully in Section. 4.

3. Setup of the tip-based nanofabrication (TBN) system

To evaluate the effectiveness of the proposed DC method, a novel TBN system is established. The setup of the system is illustrated in Fig. 3. The system mainly consists of a tip feed system, a 3-DOF nano positioning stage, and several auxiliary components.

3.1. Design of the tip feed system

The tip feed system is designed to accomplish two functions, namely, the tip-sample contact detection and the position control of the tip. Therefore, the non-contact force, i.e. the electromagnetic force is utilized. The structure of the tip feed system is shown as Fig. 3. A diamond tip is fixed on the tip support mechanism. On the reverse side of the tip support mechanism is a permanent magnet and a detection target which are assembled in series. A capacitive displacement sensor is utilized to acquire the deformation of the tip support mechanism, i.e. the displacement of the tip. A wound coil is made

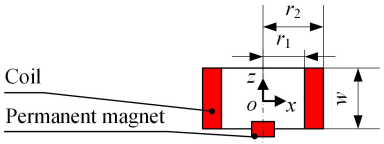

Fig. 4. Schematic diagram of the electromagnetic force driver

to provide a driving force to the permanent magnet and thus control the tip position. Therefore, a non-contact force is utilized to actuate the tip. Furthermore, a permalloy layer is used to eliminate the disturbance on the capacitive displacement sensor due to the varying current of the coil.

3.1.1. Analysis of electromagnetic force driver

By adjusting the input current, the electromagnetic force, namely, the repulsive force between the electric magnet and the permanent magnet can be controlled precisely in real-time. To analyze the magnitude of the electromagnetic force, the theoretical model of the electromagnetic actuator is illustrated in Fig. 4. The electromagnetic force F_e can be obtained by the following equation[38]:

$$F_e = B_{\text{rem}} \cdot V \cdot \frac{dH_z(z)}{dz} \tag{1}$$

where B_{rem} is the residual magnetism, V is the volume of permanent magnet, and $H_z(z)$ is the magnetic field along the axis, which can be calculated by

$$H_z(\frac{z}{r_1}) = H_z(0)\left\{\frac{f(\alpha,\beta+z/r_1)+f(\alpha,\beta-z/r_1)}{2f(\alpha,\beta)}\right\} \tag{2}$$

where

$$f(\alpha,\beta) = \beta ln\left\{\frac{\alpha+\sqrt{\alpha^2+\beta^2}}{1+\sqrt{1+\beta^2}}\right\} \tag{3}$$

$$H_z(0) = \frac{\chi NIf(\alpha,\beta)}{2r_1\beta(\alpha-1)} \tag{4}$$

In the above equation, χ, N, I is the packing factor, number of turns, and the input current of the coil, respectively, and $\alpha = r_2/r_1$ and $\beta = w/2r_1$.

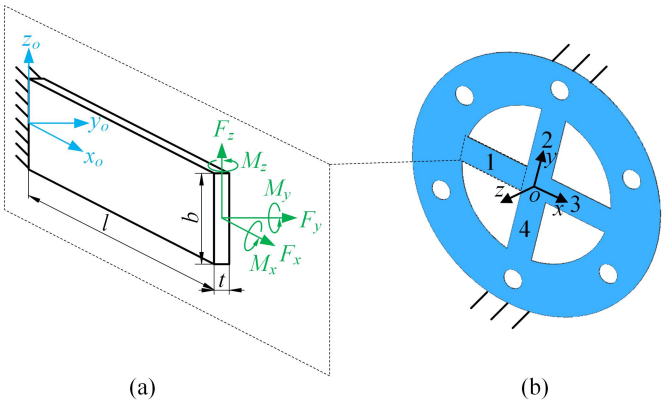

Fig. 5. (a) Model of leaf-type flexure hinge, and (b) structure of the tip support mechanism

3.1.2. Design and modelling of the tip support mechanism

A cross-shaped tip support mechanism made of beryllium bronze is designed to support the diamond tip and the permanent magnet, as shown in Fig. 5. On the one hand, increasing the flexibility of the support mechanism is beneficial for the sensitivity of the contact detection between the tip and the sample. On the other hand, high stability of the system requires a high stiffness. To choose a balanced stiffness of the cantilever support, the compliance matrix method[39] is selected due to its accuracy and convenience.

The structure of the cantilever support mechanism can be considered as a parallel kinematic mechanism made up of four cantilever beams (marked as Nos. 1/2/3/4 in Fig. 5(b). The original compliance matrix in the local coordinate as shown in Fig. 5(a) can be written as

$$C_0 = \begin{bmatrix} C_{11} & 0 & 0 & 0 & 0 & 0 \\ 0 & C_{22} & 0 & 0 & 0 & C_{26} \\ 0 & 0 & C_{33} & 0 & C_{35} & 0 \\ 0 & 0 & 0 & C_{44} & 0 & 0 \\ 0 & 0 & C_{53} & 0 & C_{55} & 0 \\ 0 & C_{62} & 0 & 0 & 0 & C_{66}, \end{bmatrix}, \tag{5}$$

where $C_{ij}(i, j = 1, 2, ..., 6)$ are the parameters of the compliance matrix.

Given an external force vector F, the displacement vector D can be obtained

Table 1: Detailed parameters of the compliance matrix

Parameters	Expression	Parameters	Expression
C_{11}	$\frac{l}{Ebt}$	C_{44}	$\frac{l}{Gk_2bt^3}$
C_{22}	$\frac{4l^3}{Ebt^3} + \frac{l}{Gbt}$	C_{53}	$-\frac{6l^2}{Eb^3t}$
C_{26}	$\frac{6l^2}{Ebt^3}$	C_{55}	$\frac{12l}{Eb^3t}$
C_{33}	$\frac{l}{Gk_2bt^3}$	C_{62}	$\frac{6l^2}{Ebt^3}$
C_{35}	$-\frac{6l^2}{Eb^3t}$	C_{66}	$\frac{12l}{Ebt^3}$

[a] l, t, b are the length, thickness, and width of cantilever beam, respectively as Fig. 5(a) depicts, and E and G are the elastic modulus and shear modulus, respectively.

[b] k_2 is a geometric parameter, $k_2 = b/t$.

by

$$D = \begin{bmatrix} x \\ y \\ z \\ \theta_x \\ \theta_y \\ \theta_z \end{bmatrix} = C \begin{bmatrix} F_x \\ F_y \\ F_z \\ M_x \\ M_y \\ M_z \end{bmatrix} = CF. \tag{6}$$

Furthermore, to transform the local compliance matrix to the global coordinate, the following equation can be used.

$$C_i = R_x^T(\alpha) R_z^T(\theta_i) C_0 R_z(\theta_i) R_x(\alpha), \tag{7}$$

where $R_x(\alpha)$ and $R_z(\theta_i)$ are the rotation matrices from local coordinate i to global coordinate.

$$R_x(\alpha) = \begin{bmatrix} 1 & 0 & 0 & 0 & 0 & 0 \\ 0 & \cos(\alpha) & -\sin(\alpha) & 0 & 0 & 0 \\ 0 & \sin(\alpha) & \cos(\alpha) & 0 & 0 & 0 \\ 0 & 0 & 0 & 1 & 0 & 0 \\ 0 & 0 & 0 & 0 & \cos(\alpha) & -\sin(\alpha) \\ 0 & 0 & 0 & 0 & \sin(\alpha) & \cos(\alpha) \end{bmatrix} \tag{8}$$

$$R_z(\theta_i) = \begin{bmatrix} \cos(\theta_i) & -\sin(\theta_i) & 0 & 0 & 0 & 0 \\ \sin(\theta_i) & \cos(\theta_i) & 0 & 0 & 0 & 0 \\ 0 & 0 & 1 & 0 & 0 & 0 \\ 0 & 0 & 0 & \cos(\theta_i) & -\sin(\theta_i) & 0 \\ 0 & 0 & 0 & 0 & \sin(\theta_i) & \cos(\theta_i) \\ 0 & 0 & 0 & 0 & 0 & 1 \end{bmatrix} \tag{9}$$

The rotation angle $\alpha(=-\pi/2)$ and $\theta_i(=(i-1)\cdot\pi/2, i=1,2,3,4)$ are defined as the rotation angle about the x and z axes respectively from local coordinate to the global coordinates.

According to [39], for parallel connection the stiffness in the center of the support mechanism

$$K_{\mathrm{c}} = \sum_{i=1}^{n} K_i (i = 1, 2, 3, 4), \tag{10}$$

where the stiffness matrix of ith cantilever beam $K_i = C_i^{-1}$ is the inverse of the corresponding compliance matrix.

With the selected geometric parameters, the stiffness in the vertical direction of the tip support mechanism is 0.0031 N/μm. The stiffness can satisfy the requirements of detection sensitivity of the tip-sample contact and the dynamic performance.

3.2. 3-DOF nano positioner

In the developed TBN system, a 3-DOF nano positioner is employed to accomplish the scratching motion as shown in Fig. 3. A z stage is serially connected on the output end of an xy stage. The z stage can be used to drive the sample to contact the tip, while the xy stage can provide the relative motion between the sample and the tip to machine arbitrary 2D/3D patterns.

3.3. Auxiliary components

As well as the above key components, several auxiliary components are also essential. As shown in Fig. 3, a manual xyz platform is used to accomplish the coarse positioning between the tip and the sample. In order to diminish the angle of inclination of the sample surface, a $\theta_x\theta_y$ angle adjusting platform is employed.

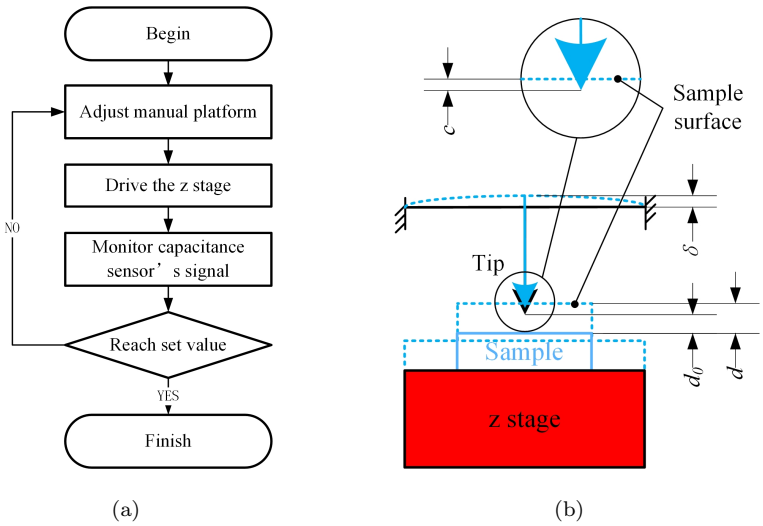

Fig. 6. (a) Flow chart and (b) schematic diagram of contact detection between the tip and the sample

With the help of a gradienter, the initial angle can be adjusted preliminarily into an acceptable range. The tip feed system is mounted on the xyz manual platform to provide the feed motion of the tip. A 3-DOF nano positioner is utilized to realize the relative motion, and to accomplish the contact detection between the tip and the sample surface. All the components are fitted on a base to form a completed integrated system.

4. Machining procedure

Based on the TBN system, the machining procedure to implement the DC method is enumerated as follows:

4.1. Pre-scan of the sample surface

As mentioned above, the inclination of the sample surface can lead to the gradually changing machining depth. To solve this problem, a novel active compensation method is proposed. The method is based on the contact detection between the tip and the sample. Fig. 6(a) shows the flow chart which depicts

the operation sequence, and Fig. 6(b) shows the schematic diagram. As the output displacement of z stage is limited to 17.45 μm, trial and error method is adopted with the help of the manual platform. The sample surface approaches the tip driven by the manual platform and the z stage, until the signal of the capacitive sensor reaches a set value δ. In the last loop of this process, the relationship between the initial distance d_0, the displacement of sample surface d, the deformation of cantilever support δ, and the indentation depth c, can be expressed as

$$d = d_0 + \delta + c. \tag{11}$$

As the indentation depth is proportional to the normal force F_n applied on the sample surface by the tip, namely,

$$c = k \cdot F_n, \tag{12}$$

where k is a coefficient determined by the contact conditions.

According to Newton's third law, the following equation can be obtained.

$$F_n = K_z \cdot \delta \tag{13}$$

where K_z is the vertical stiffness of the tip support mechanism.

Substituting Eqs. (12) and (13) into Eq. (11), Eq. (11) can be transformed into

$$d_0 = d - (1 + kK_z)\delta \tag{14}$$

It can be seen that the initial distance d_0 between the tip and the sample at a certain point can be obtained by recording the move distance d.

Thus, by measuring the distance $d_{0i}(i = 1, 2, ..., n)$ at a series of points $(P_i, i = 1, 2, ..., n)$ on the sample surface, the equation of the plane, namely, the space angle, of the sample surface can be fitted as illustrated in Fig. 7. This process is referred to as pre-scan.

4.2. Machining process with active compensation

In the previous step, a fitted plane in the local coordinates of the tip position can be obtained. Afterwards, the distance variation information in the

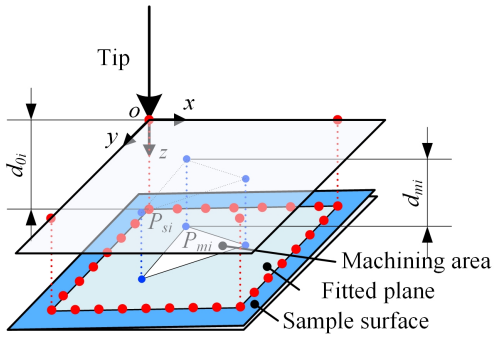

Fig. 7. Schematic diagram of plane fit and machining with active compensation

machining area can be calculated by the corresponding xy coordinates as shown in Fig. 7. In the machining process, the obtained distance information along the machining path is employed to control feeding distance of tip, which is driven by the electromagnetic actuator. Under the action of the electromagnetic force, the tip will indent into the sample surface. The distance the tip moves by

$$d = d_0 + D_m, \tag{15}$$

where D_m is the stated machining depth.

To fabricate a complicated 2D/3D patterns, the relative motion with specific trajectory between the tip and the sample will be accomplished by the xy stage. At the same time, the tip feed system accomplishes the active compensation by adjusting the tip position according to the height information of the sample surface.

4.3. Post processing

After finishing the machining process, the sample will go through an ultrasonic cleaning in alcohol for ten minutes to clean off the machining chips. Then the surface topography will be measured and imaged by AFM.

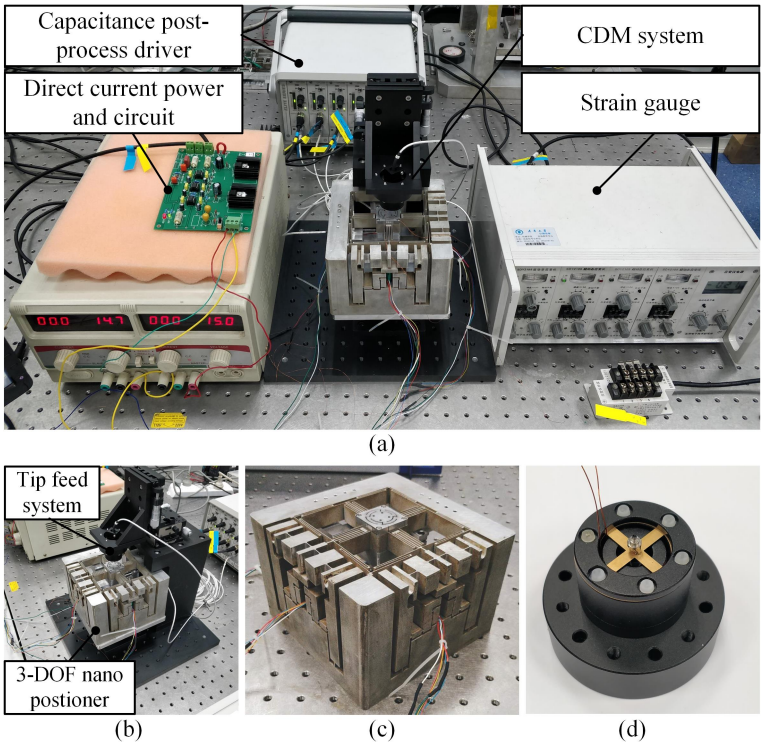

Fig. 8. Experimental setup: (a) the overall structure, (b) the DC system, (c) the 3-DOF nano postioner, and (d) the tip feed system

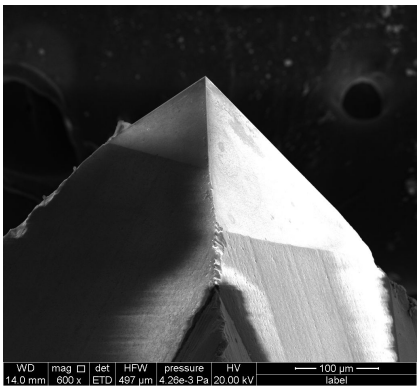

Fig. 9. Diamond tip's picture taken by scanning electron microscope (SEM)

5. Experimental investigation

5.1. Experimental setup and characterization

To evaluate and investigate the effectiveness of the proposed 3D TBN system and the DC method, a series of experiments were conducted.

The experimental setup is illustrated in Fig. 8. The xyz manual platform has a full range of 13 mm and resolution of 0.5 μm in the three coordinate directions (model: WN304ZM13M, from Winner Optical Instruments Group Company Ltd., China). The $\theta_x\theta_y$ angle adjusting platform has a full range of 2° and resolution of 30″ (model: WN03GM10 and WN04GM15, from Winner Optical Instruments Group Company Ltd., China). The tip feed system is actuated by a direct current power supply and an in-house developed circuit. The xy stage and z stage are closed-loop controlled by proportional-integral-derivative (PID) control algorithm. Three piezoelectric actuators (model: PZS001, from THORLABS Company, America) are utilized to provide required input displacements. Two capacitive displacement sensors (model: CPL290, from LION PRECISION, USA) and a strain gauge are used to measure the displacements of the stage. The capacitive displacement sensors have a selectable range of 25 μm or 100 μm with resolution of 0.004% of the full range, i.e. 1 nm/ 4nm. Additionally, as the machining tool, a three-sided pyramidal diamond tip (model: Cubecorner, from Synton-MDP LTD, Switzerland) with a face angle of 35.26° and a nominal stylus radius of 150 nm is adopted as shown in Fig. 9. All the control algorithms are implemented using the dSPACE DS1103 R&D control board. The control program is written in the MATLAB/Simulink environment, and then downloaded into the dSPACE board.

5.1.1. The performance tests of the tip feed system

The tip feed system is designed to dynamically adjust the tip displacement. Its output and tracking performance are extremely important. The experimental results of four tests, namely, the output range, step response, motion resolution, and motion tracking performance, are illustrated in Fig. 10 (a) -

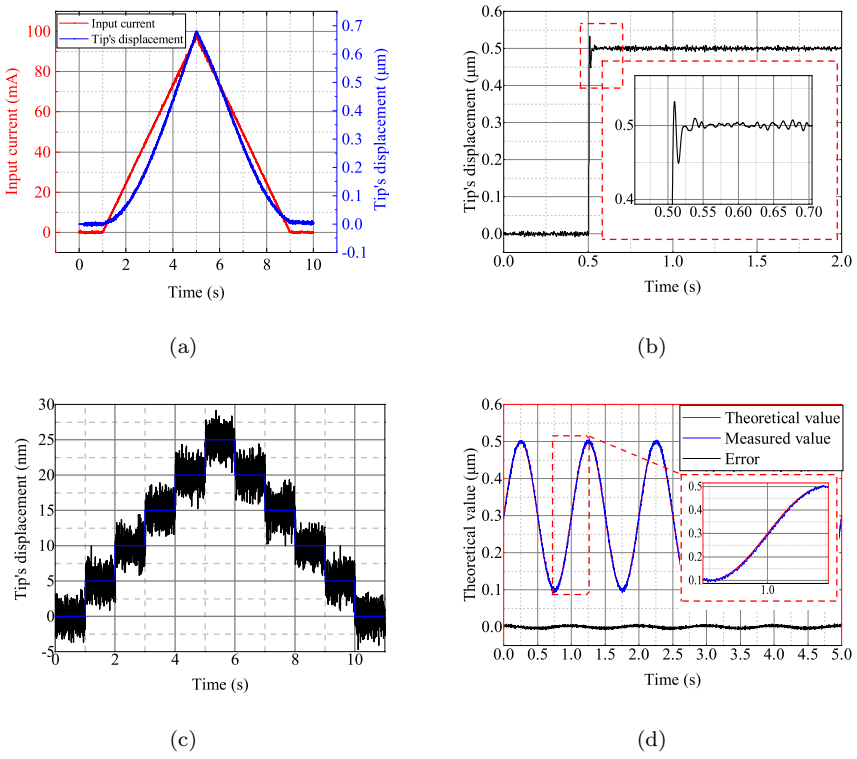

Fig. 10. Experimental results of performance tests of the tip feed system: (a) the output range, (b) the step response, (c) the motion resolution, and (d) the motion tracking performance

(d), respectively. Results show that the output range can reach up to 0.7 μm at a current of 100 mA. It can be seen that there is a nonlinear relationship between the input current and the output displacement. To address this issue, a PID feedback controller is utilized. It can be seen that the settling time of the step response test is about 23 ms, which ensures a fast response. Furthermore, the results demonstrate that the resolution can reach 5 nm and the tracking error of a sinusoidal signal at 1 Hz is 2.5%.

5.1.2. The performance tests of the 3-DOF nano positioner

To examine the characteristics of the DC system, a number of verification tests have been conducted. Fig. 11 shows that the output range of the 3-DOF

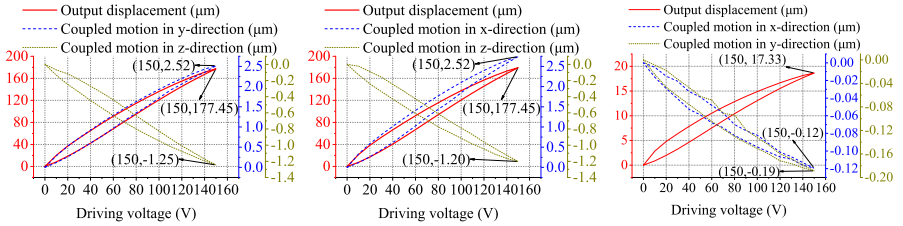

(a) (b) (c)

Fig. 11. Experimental results of the motion ranges and the coupled motions in: (a) x axis, (b) y axis, and (c) z axis

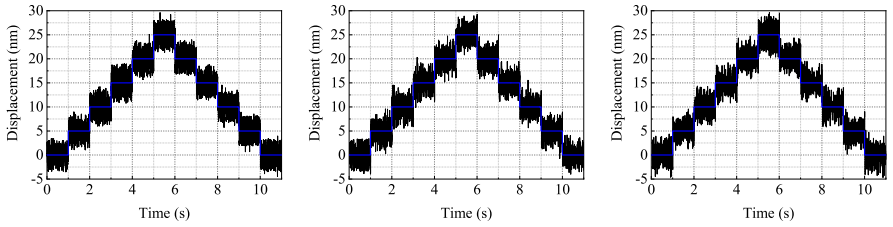

(a) (b) (c)

Fig. 12. Experimental results of the resolution test in: (a) x axis, (b) y axis, and (c) z axis

nano positioner in the $x/y/z$ axis can reach up to 177.33 μm, 179.30 μm, and 17.45 μm, respectively. Moreover the motion resolution can all reach up to 5 nm as illustrated in Fig. 12.

5.2. Pre-scan process

The pre-scan process is accomplished by repeating the contact detection at several preset points. When the sample approaches the tip with the z stage, the distance between tip and sample surface can be obtained by recording the displacement of the stage. The velocity of z stage is set as 1 $\mu m/s$. The results of the pre-scan process and the fitted plane are shown in Fig. 13. It can be seen that the fitted surface is a space plane with an equation of $z = z0 + a * x + b * y$, where $z0$, a and b are the undetermined coefficients. In the machining process, the fitted plane will be used to compensate the tilt angle and the coupling errors.

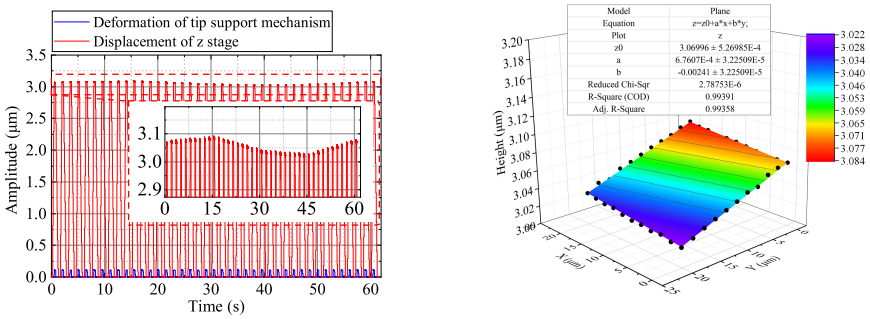

(a) (b)

Fig. 13. (a) Results of the pre-scan process, and (b) the fitted plane

5.3. Nanofabrication experiments

To further verify the nanofabrication ability, a series of experiments were conducted. The nano grooves were fabricated by single scan at a speed of 5 μm/s. Afterwards, the fabricated patterns were imaged by AFM (model: CSPM5500, from Being Nano-Instruments, China).

5.3.1. Results of the active compensation

To validate the effectiveness of the active compensation, a contrast experiment was conducted on a silicon surface. Fig. 14 illustrates the AFM image and the depth information along the length of the groove. Fig. 14(a) reveals the machining result without the active compensation. Due to the tilt angle between the sample surface and the horizontal plane, the machining depth grows deeper if the tip is kept at a constant height. As a contrast, the machining depth is well controlled under active compensation condition as shown in Fig. 14(c) when the height information is applied to adjust the tip position dynamically. It should be noted that the coupling error in the z axis from the x and y axes are also compensated, as the pre-scan process is accomplished by the xy stage with the same trajectory. Therefore, the fitted plane is the combination of sample surface and the coupling error.

5.3.2. Results of depth control

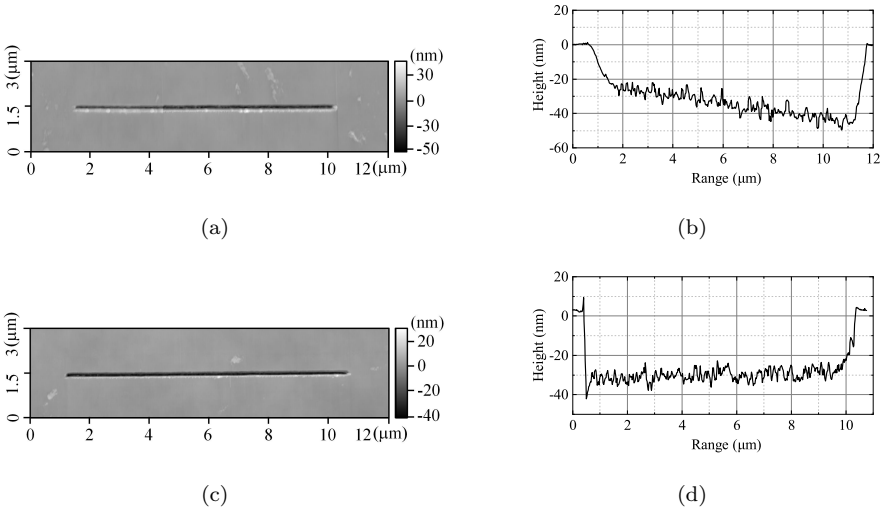

Fig. 14. AFM images and depth information along the length of the groove fabricated without (a), (b) and with (c), (d) the active compensation

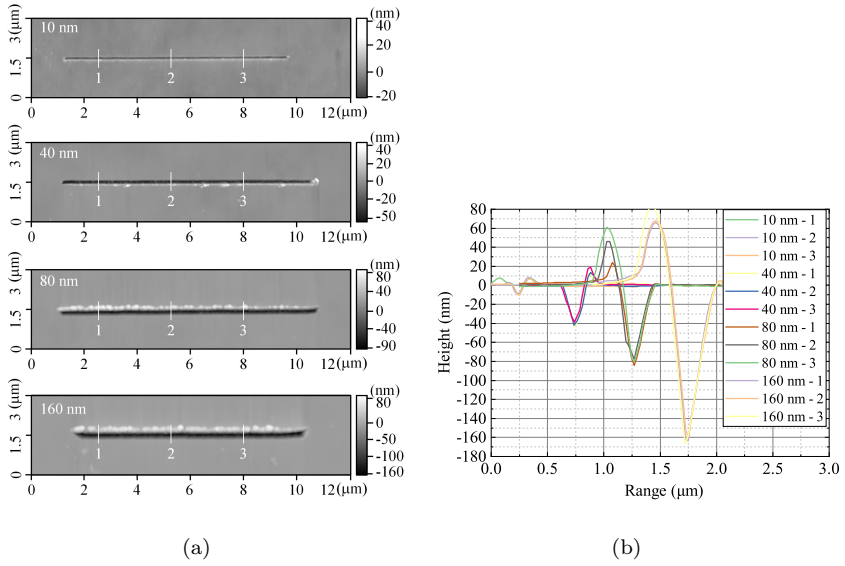

Fig. 15. (a) AFM images and (b) cross-section profiles of the nano grooves of different machining depths

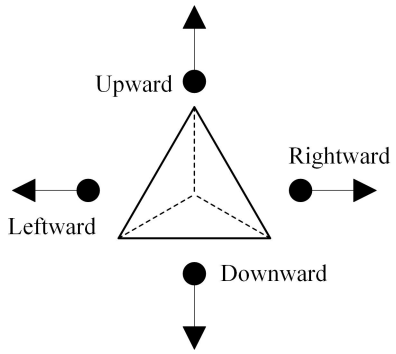

Fig. 16. Schematic diagram of different machining directions

Verification of machining depth controllability. In order to demonstrate the machining depth controllability, four nano-grooves, with different depth values, namely, 10 nm, 40 nm, 80 nm, and 160 nm, were fabricated. For each case, the rest of the machining parameters are kept consistent. The experimental results are shown in Fig. 15. Fig. 15(a) illustrates the AFM image, while Fig. 15(b) illustrates the cross-section profiles of the nanofabrication grooves of different machining depths, respectively. It can be observed that the machining depths are well-controlled. Moreover, the maximum machining depth reaches 160 nm, which is much larger than the depth obtained by AFM. However, it should be noted that as the depth increases, more material accumulates on the edge of the groove. Fig. 15(b) shows that the peak has reach about 70 nm when the depth is 160 nm. According to literature, there are mainly two deformation forms during the scratching process, including ploughing and cutting forms[40, 41]. When the attack angle between the sample surface and the tip is greater than 75°, the predominant deformation form will be in the cutting state[42, 43]. In this research, the attack angle is no more than 35.26°, which is the face angle of the diamond tip. Therefore, the predominant deformation state will be the ploughing state. As a result, the material piles up on the sides of the tip, forming a side-flow. Since the machining direction is along the horizontal direction, i.e. the leftward or the rightward direction as illustrated in Fig. 16, the material flow accumulates on the upside of the fabricated groove. Similar results can be seen

from references [15] and [36].

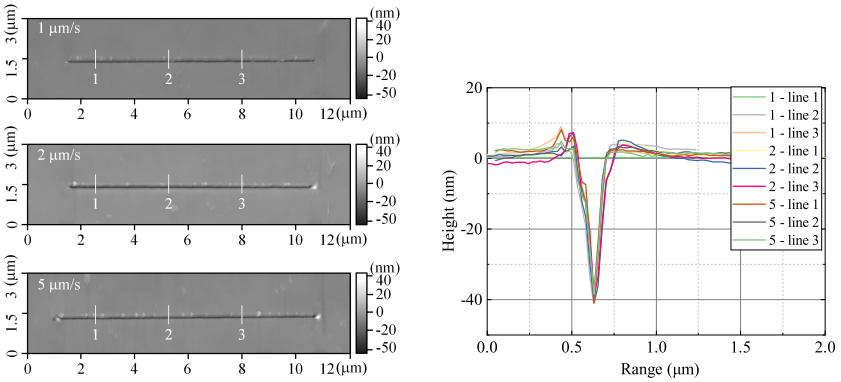

(a) (b)

Fig. 17. (a) AFM images and (b) cross-section profiles of the nanofabrication results at different machining speeds

Verification of different machining speeds. Recent research efforts reveal that both the cutting force and normal force increase with the increasing of machine speed[40, 44]. This is due to the fact that the dislocations have less time to move away from the cutting region at a higher cutting velocity. Therefore, the pile-up dislocations in the cutting region strengthen the materials and larger cutting force and normal force are required. Besides, a higher cutting velocity results in a larger resistance to motion due to a enlarged chip volume, thus leads to a increased cutting force. Hence, the FC method may lead to the variation of the machining depth. To verify the influence of speed with the DC method on machining depth, three lines with different machining speeds of 1 μm/s, 2 μm/s, and 5 μm/s, respectively were fabricated. Fig. 17 illustrates the AFM images and the cross-section profiles of the nanofabrication grooves at different machining speeds. The results show that within the limited range of variation, the machine speed has little influence on the machining depth.

Verification of different machining directions. Another key machining parameter that will affect machining depth is the machining direction, as the diamond

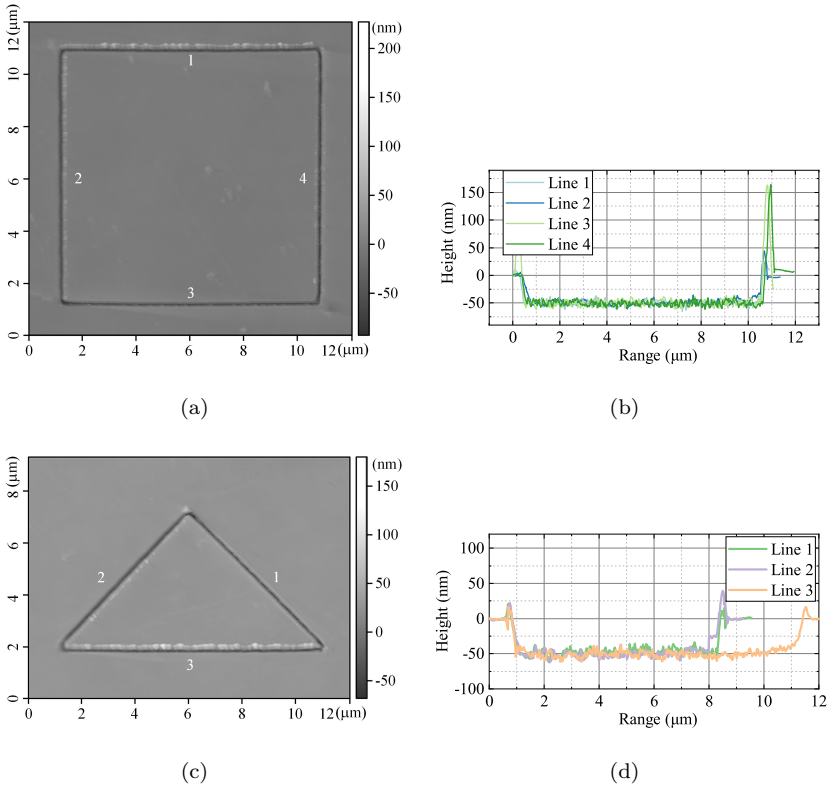

Fig. 18. AFM images (a), (c) and depth information along the length of grooves (b), (d) of a square and a right triangle

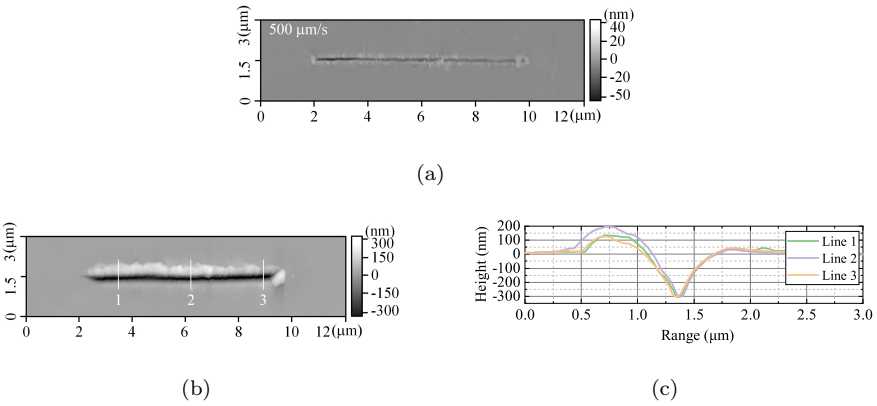

Fig. 19. (a) AFM image of the groove fabricated at machining speed of 500 μm/s, (b) and (c) AFM image and cross-section profile of the groove with depth of 300 nm

tip has a three-sided pyramidal shape. To verify the proposed DC method, an experiment was conducted. A square pattern and a right triangle pattern were machined end to end with a pre-set depth of 50 nm, hence, four major machining directions are taken into consideration. Fig. 18 shows the nanofabrication results of different machining directions, including the AFM image and the depth information along the length of grooves. The machining depths of nano grooves in each direction have a uniform mean value, which verifies the depth controllability of the DC method.

5.3.3. Results of maximum machining speed and maximum machining depth

To verify the machining ability of the developed TBN system, the maximum machining speed and maximum machining depth were tested. Fig. 19 (a) shows the AFM image of the groove fabricated at machining speed of 500 μm/s, while Fig. 19 (b) and (c) show the AFM image and the cross-section profile of the groove with depth of 300 nm. It can be seen that the consistency of fabricated groove drops noticeably, when the machining speed reaches to about 500 m/s, or the depth 300 nm, .

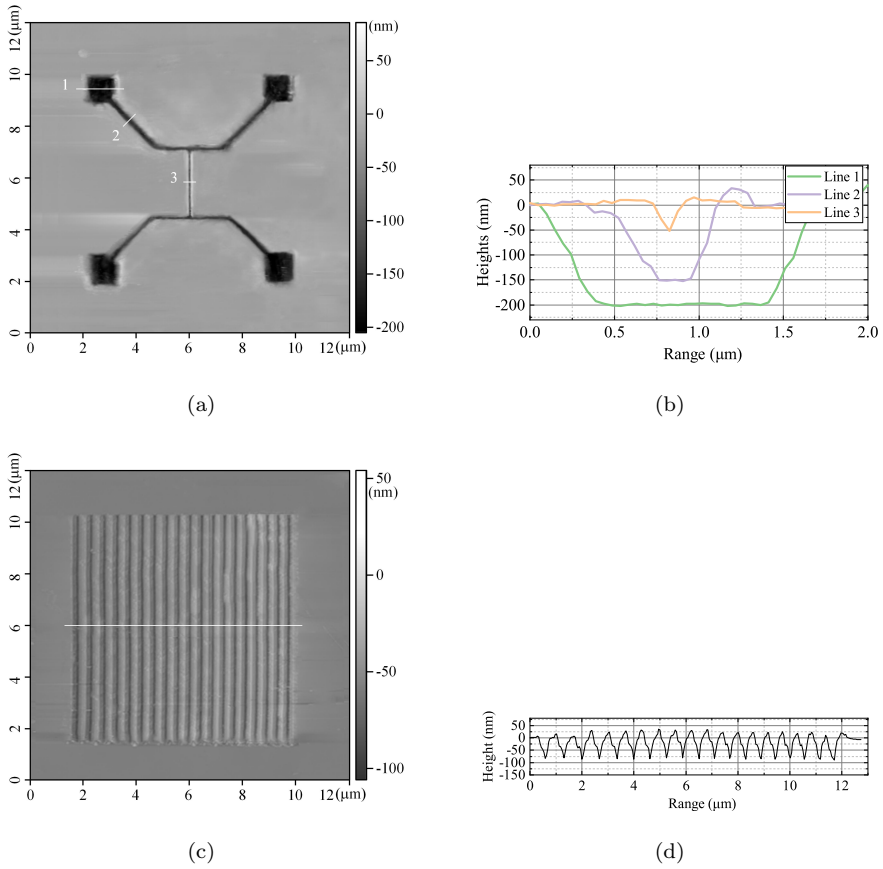

Fig. 20. AFM images (a), (c) and cross-section profiles (b), (d) of nanochannels for micro/nanofluidic systems

5.3.4. Results of nanochannels and complicated patterns

In order to obtain further insight into the machining capability, two typical kinds of nanochannels for micro/nanofluidic systems (as shown in Fig. 20)and a complicated 3D pattern, i.e. a photochrome (as shown in Fig. 21), were fabricated. For the fabrication of the 3D pattern, firstly, the photos are converted to grayscales. Every pixel of the grayscale is related to the machining depth in the local coordinate. Finally, the image is fabricated column by column with a feed of 50 nm. The AFM image and the cross-section profiles of two kinds of nanochannels are illustrated in Fig. 20. It can be seen that the machining

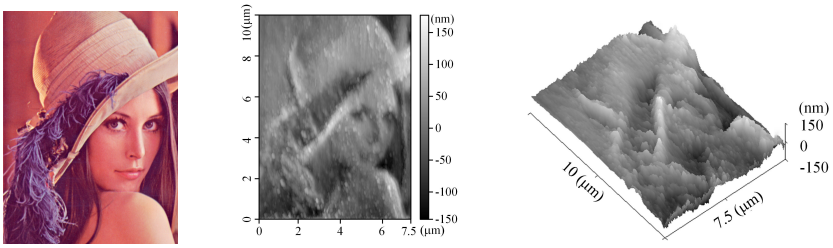

(a) (b) (c)

Fig. 21. Verification of complicated 3D pattern: (a) a photochrome, (b) 2D view and (c) 3D view of the AFM image

Table 2: Comparison of existing TBN systems

	Tip type	Sample material	Machining area	Maximum machining depth	Maximum machining speed	Machining precision	In situ image ability
[17]	Diamond tip with cantilever	Aluminum	100 μm × 100 μm	200 nm	10 μm/s	±5 nm	Yes
[45]	Single crystal diamond probe	Soda-lime glass	/	25 nm	5 μm/s	/	Yes
[36]	Berkovich diamond tip	Silicon	10 μm × 10 μm	70 nm	10 μm/s	±20 nm	No
This work	Cubecorner diamond tip	Silicon	177 μm × 179 μm	300 nm	500 μm/s	± 5 nm	No

depths are well controlled at different section of the nanochannels. The fabricated photochrome and the 2D/3D view of the AFM image are illustrated in Fig. 21. The machining result shows that the photo is copied to the silicon sample in a size of 10 μm × 10 μm with clear details.

6. Discussion

The experimental results demonstrate the machining capability of the novel 3D TBN system for high precision depth control. To show the difference between the proposed system and existing TBN systems, a comparison has been made as illustrated in TABLE 2. It can be seen that a larger machining area

is achieved by utilizing the 3-DOF nano positioner. Additionally, the maximum machining range and machining precision of patterns on silicon surface have been improved. However, the system sacrifices the in situ image ability due to the large stiffness of the tip support mechanism.

Nevertheless, some issues should be pointed out. Firstly, the DC method needs an additional procedure, i.e. the pre-scan process, which adds to the complexity. Moreover, the systematic error resulting from the plane fitting will affect the depth control capability. The main reason is that the detection forces have a few deviations, which are difficult to eliminate. Therefore, a more sensitive height detection method, e.g. a tip support mechanism with higher compliance, is required. Secondly, the material accumulation increases with the machining depths, especially when the depth is larger than 60 nm. However, this phenomenon is an inherent problem of mechanical scratching. In the future work, reducing or even eliminating the material accumulation will be a major research direction.

7. Conclusion

In summary, a novel 3D TBN system for high precision depth control is established and validated in this paper. The tip feed system utilizes the electromagnetic force, to adjust the tip displacement. The non-contact force accomplishes the combination of the tip-sample contact detection and the tip actuation. The proposed DC method decreases the complexity and high uncertainty of the force-depth prediction, which may depend on removal speed, direction, and material properties, etc. with the FC method. Furthermore, the active compensation method is proposed to eliminate the tilt angle between the sample surface and the horizontal plane. Silicon sample is selected for the machining tests as it has large hardness. To verify the accuracy and effectiveness of the tip-sample contact detection and pre-scan process, a comparison between with and without the active compensation method is conducted. Based on the DC method, grooves and other patterns are fabricated. The maximum depth

of a single scan can reach up to 300 nm, which is much larger than AFM-based fabrication system. Moreover, the fabricated square pattern shows that the DC method eliminate the inconformity of different machining directions. The experimental results demonstrate that the the developed 3D TBN system is capable of good accuracy, repeatability, and robustness, i.e. reduce/eliminate the influence of the above-mentioned factors on the machining depth.

Acknowledgements

This research is supported by National Natural Science Foundation of China (Nos. 51675371, 51675367 and 51675376), National Key R&D Program of China (Nos. 2017YFB1104700, 2017YFE0112100, and 2016YFE0112100), China-EU H2020 MNR4SCell (No.734174).

References

[1] J. Han, H. G. Craighead, Separation of long dna molecules in a microfabricated entropic trap array, Science 288 (5468) (2000) 1026–1029. doi:10.1126/science.288.5468.1026.

[2] Y. Hu, Y. Zhang, C. Xu, L. Lin, R. L. Snyder, Z. L. Wang, Self-powered system with wireless data transmission, Nano Letters 11 (6) (2011) 2572–2577. doi:10.1021/nl201505c.

[3] E. Eleftheriou, Nanopositioning for storage applications, Annual Reviews in Control 36 (2) (2012) 244–254. doi:10.1016/j.arcontrol.2012.09.006.

[4] X. Pan, X. Zhao, J. Chen, A. Bermak, Z. Fan, A fast-response/recovery zno hierarchical nanostructure based gas sensor with ultra-high room-temperature output response, Sensors and Actuators B: Chemical 206 (2015) 764–771. doi:https://doi.org/10.1016/j.snb.2014.08.089.

[5] Y. Yuan, D. Zhang, X. Jing, H. Zhu, W.-L. Zhu, J. Cao, K. F. Ehmann, Fabrication of hierarchical freeform surfaces by 2d compliant vibration-

assisted cutting, International Journal of Mechanical Sciences 152 (2019) 454–464. doi:10.1016/j.ijmecsci.2018.12.051.

[6] K. Mohamed, M. M. Alkaisi, Investigation of a nanofabrication process to achieve high aspect-ratio nanostructures on a quartz substrate, Nanotechnology 24 (1) (2013) 015302. doi:10.1088/0957-4484/24/1/015302.

[7] J. Jeon, H. C. Floresca, M. J. Kim, Fabrication of complex three-dimensional nanostructures using focused ion beam and nanomanipulation, Journal of Vacuum Science & Technology B 28 (3) (2010) 549–553. doi:10.1116/1.3406134.

[8] R. R. Gattass, E. Mazur, Femtosecond laser micromachining in transparent materials., Nature Photonics 2 (4) (2008) 219–225. doi:10.1038/nphoton.2008.47.

[9] P. Dumon, W. Bogaerts, V. Wiaux, J. Wouters, S. Beckx, J. Van Campenhout, D. Taillaert, B. Luyssaert, P. Bienstman, D. Van Thourhout, R. Baets, Low-loss soi photonic wires and ring resonators fabricated with deep uv lithography, IEEE Photonics Technology Letters 16 (5) (2004) 1328–1330. doi:10.1109/LPT.2004.826025.

[10] J. R. Maldonado, M. Peckerar, X-ray lithography: Some history, current status and future prospects, Microelectronic Engineering 161 (2016) 87–93. doi:10.1016/j.mee.2016.03.052.

[11] N. Unno, J. Taniguchi, Y. Ishii, Sub-100-nm three-dimensional nanoimprint lithography, Journal of Vacuum Science & Technology B: Microelectronics and Nanometer Structures 25 (6) (2007) 2361. doi:10.1116/1.2811715.

[12] S. Hong, J. Zhu, C. A. Mirkin, Multiple ink nanolithography: toward a multiple-pen nano-plotter, Science 286 (5439) (1999) 523–525. doi:10.1126/science.286.5439.523.

[13] Y. Yan, Y. Geng, Z. Hu, Recent advances in AFM tip-based nanomechanical machining, International Journal of Machine Tools and Manufacture 99 (2015) 1–18. doi:10.1016/j.ijmachtools.2015.09.004.

[14] A. A. Tseng, Three-dimensional patterning of nanostructures using atomic force microscopes, Journal of Vacuum Science & Technology B 29 (29) (2011) 040801. doi:10.1116/1.3609921.

[15] A. A. Tseng, C.-F. J. Kuo, S. Jou, S. Nishimura, J.-i. Shirakashi, Scratch direction and threshold force in nanoscale scratching using atomic force microscopes, Applied Surface Science 257 (22) (2011) 9243–9250. doi:10.1016/j.apsusc.2011.04.065.

[16] Z.-C. Lin, H.-Y. Jheng, H.-Y. Ding, An innovative method and experiment for fabricating bulgy shape nanochannel using AFM, Applied Surface Science 347 (2015) 347–358. doi:10.1016/j.apsusc.2015.04.042.

[17] Y. Yan, Z. Hu, X. Zhao, T. Sun, S. Dong, X. Li, Top-down nanomechanical machining of three-dimensional nanostructures by atomic force microscopy, Small 6 (6) (2010) 724–728. doi:10.1002/small.200901947.

[18] M. Malekian, S. S. Park, D. Strathearn, M. G. Mostofa, M. B. G. Jun, Atomic force microscope probe-based nanometric scribing, Journal of Micromechanics and Microengineering 20 (11) (2010) 115016. doi:10.1088/0960-1317/20/11/115016.

[19] S. Chung, J. H. Lee, M. O. Moon, J. Han, R. D. Kamm, Non-lithographic wrinkle nanochannels for protein preconcentration, Advanced Materials 20 (16) (2008) 3011–3016. doi:10.1002/adma.200701715.

[20] S. M. Park, Y. S. Huh, H. G. Craighead, D. Erickson, A method for nanofluidic device prototyping using elastomeric collapse, Proceedings of the National Academy of Sciences of the United States of America 106 (37) (2009) 15549–15554. doi:10.1073/pnas.0904004106,10.1073/pnas.0904004106.

[21] X. Liang, S. Y. Chou, Nanogap detector inside nanofluidic channel for fast real-time label-free DNA analysis, Nano Letters 8 (5) (2008) 1472–1476. doi:10.1021/nl080473k.

[22] F. Martin, R. Walczak, A. Boiarski, M. Cohen, T. West, C. Cosentino, M. Ferrari, Tailoring width of microfabricated nanochannels to solute size can be used to control diffusion kinetics, Journal of Controlled Release 102 (1) (2005) 123–133. doi:10.1016/j.jconrel.2004.09.024.

[23] S. Xiong, L. K. Chin, K. Ando, T. Tandiono, A. Q. Liu, C. D. Ohl, Droplet generation via a single bubble transformation in a nanofluidic channel, Lab on A Chip 15 (6) (2015) 1451–1457. doi:10.1039/c4lc01184h.

[24] W. Sparreboom, A. V. D. Berg, J. C. T. Eijkel, Transport in nanofluidic systems: a review of theory and applications, New Journal of Physics 12 (3) (2010) 338–346. doi:10.1088/1367-2630/12/1/015004.

[25] H. Spelthahn, A. Poghossian, M. J. Sch?ning, Self-aligned nanogaps and nanochannels via conventional photolithography and pattern-size reduction technique, Electrochimica Acta 54 (25) (2009) 6010–6014. doi:10.1016/j.electacta.2009.03.029.

[26] A. A. Evstrapov, I. S. Mukhin, A. S. Bukatin, I. V. Kukhtevich, Ion and electron beam assisted fabrication of nanostructures integrated in microfluidic chips, Nuclear Instruments and Methods in Physics Research Section B: Beam Interactions with Materials and Atoms 282 (2012) 145–148. doi:10.1016/j.nimb.2011.08.035.

[27] M. A. Rad, K. Ibrahim, Fabrication of 20 nm deep silicon dioxide channel using electron beam lithography for manipulation of dna molecules, in: International Conference on Enabling Science & Nanotechnology, 2012, pp. 1–2. doi:10.1109/ESciNano.2012.6149651.

[28] X. Liang, K. J. Morton, R. H. Austin, S. Y. Chou, Single sub-20 nm wide, centimeter-long nanofluidic channel fabricated by novel nanoimprint mold

fabrication and direct imprinting, Nano Letters 34 (12) (2007) 3774–3780. doi:10.1021/nl072253x.

[29] Z. Ran, J. Chu, Q. Wang, Z. Wang, C. Yan, Fabrication of nanochannels using underexposed nanoimprint method, Micro & Nano Letters 10 (1) (2015) 34–36. doi:10.1049/mnl.2014.0412.

[30] M. Ringger, H. R. Hidber, R. Schlogl, P. Oelhafen, H. J. Guntherodt, Nanometer lithography with the scanning tunneling microscope, Applied Physics Letters 46 (9) (1985) 832–834. doi:10.1063/1.95900.

[31] A. A. Tseng, Advancements and challenges in development of atomic force microscopy for nanofabrication, Nano Today 6 (5) (2011) 493–509. doi:10.1016/j.nantod.2011.08.003.

[32] D. Pires, J. L. Hedrick, A. D. Silva, J. Frommer, B. Gotsmann, H. Wolf, M. Despont, U. Duerig, A. W. Knoll, Nanoscale three-dimensional patterning of molecular resists by scanning probes, Science 328 (5979) (2010) 732–735. doi:10.1126/science.1187851.

[33] X. N. Xie, H. J. Chung, C. H. Sow, A. T. S. Wee, Nanoscale materials patterning and engineering by atomic force microscopy nanolithography, Materials Science and Engineering: R: Reports 54 (1-2) (2006) 1–48. doi:10.1016/j.mser.2006.10.001.

[34] A. P. Malshe, K. P. Rajurkar, K. R. Virwani, C. R. Taylor, D. L. Bourell, G. Levy, M. M. Sundaram, J. A. McGeough, V. Kalyanasundaram, A. N. Samant, Tip-based nanomanufacturing by electrical, chemical, mechanical and thermal processes, CIRP Annals - Manufacturing Technology 59 (2) (2010) 628–651. doi:10.1016/j.cirp.2010.05.006.

[35] H. Gőbel, P. von Blanckenhagen, Atomic force microscope as a tool for metal surface modifications, Journal of Vacuum Science & Technology B: Microelectronics and Nanometer Structures Processing, Measurement, and Phenomena 13 (3) (1995) 1247–1251. doi:10.1116/1.588245.

[36] Z. Guo, Y. Tian, X. Liu, F. Wang, C. Zhou, D. Zhang, Experimental investigation of the tip based micro/nano machining, Applied Surface Science 426 (2017) 406–417. doi:10.1016/j.apsusc.2017.07.181.

[37] B. A. Gozen, O. B. Ozdoganlar, Design and evaluation of a mechanical nanomanufacturing system for nanomilling, Precision Engineering 36 (1) (2012) 19–30. doi:10.1016/j.precisioneng.2011.06.001.

[38] S. T. Smith, D. G. Chetwynd, An optimized magnet-coil force actuator and its application to precision elastic mechanisms, Proceedings of the Institution of Mechanical Engineers Part C Journal of Mechanical Engineering Science 204 (43) (1990) 243–253. doi:10.1243/PIME_PROC_1990_204_102_02.

[39] H.-H. Pham, I.-M. Chen, Stiffness modeling of flexure parallel mechanism, Precision Engineering 29 (4) (2005) 467–478. doi:10.1016/j.precisioneng.2004.12.006.

[40] P.-z. Zhu, Y.-z. Hu, T.-b. Ma, H. Wang, Study of AFM-based nanometric cutting process using molecular dynamics, Applied Surface Science 256 (23) (2010) 7160–7165. doi:10.1016/j.apsusc.2010.05.044.

[41] J. Zhang, T. Sun, Y. Yan, Y. Liang, Molecular dynamics study of scratching velocity dependency in afm-based nanometric scratching process, Materials Science and Engineering: A 505 (1) (2009) 65–69. doi:10.1016/j.msea.2008.10.049.

[42] Y. Yan, T. Sun, Y. Liang, S. Dong, Investigation on AFM-based micro/nano-cnc machining system, International Journal of Machine Tools and Manufacture 47 (11) (2007) 1651–1659. doi:10.1016/j.ijmachtools.2007.01.008.

[43] V. N. Koinkar, B. Bhushan, Scanning and transmission electron microscopies of single-crystal silicon microworn/machined using atomic force mi-

croscopy, Journal of Materials Research 12 (12) (1997) 3219–3224. doi:10.1557/jmr.1997.0421.

[44] Q. X. Pei, C. Lu, H. P. Lee, Large scale molecular dynamics study of nanometric machining of copper, Computational Materials Science 41 (2) (2007) 177–185. doi:10.1016/j.commatsci.2007.04.008.

[45] M. G. Mostofa, C. I. Park, S. S. Park, AFM probe based nano mechanical scribing of soda-lime glass, Journal of Manufacturing Processes 15 (4) (2013) 625–634. doi:10.1016/j.jmapro.2013.05.003.